Check for updates

Magnetic Resonance in Medicine

WILEY | ISMRM ONE COMMUNITY FOR CLINICIANS AND SCIENTISTS

RESEARCH ARTICLE OPEN ACCESS

Time-Resolved 3D Imaging and Strain Analysis of the Skeletal Muscle

Max H. C. van Riel[1] | David G. J. Heesterbeek[1] | Martijn Froeling[2] | Tristan van Leeuwen[3,4] | Cornelis A. T. van den Berg[1] | Alessandro Sbrizzi[1]

[1]Computational Imaging Group for MRI Therapy & Diagnostics, Department of Radiotherapy, University Medical Center Utrecht, Utrecht, the Netherlands | [2]Precision Imaging Group, Department of Radiology, University Medical Center Utrecht, Utrecht, the Netherlands | [3]Mathematical Institute, Utrecht University, Utrecht, the Netherlands | [4]Computational Imaging Group, Centrum Wiskunde & Informatica, Amsterdam, the Netherlands

Correspondence: Max H. C. van Riel (m.h.c.vanriel-3@umcutrecht.nl)

Received: 23 July 2026 | **Revised:** 8 October 2026 | **Accepted:** 27 October 2026

Keywords: 4D MRI | biomechanics | dynamics | motion | muscle | strain

ABSTRACT

Purpose: To develop and validate a method for time-resolved 3D imaging and strain analysis that enables quantification of dynamic in vivo muscle deformations from aperiodic continuous motion.

Theory and Methods: Controlled deformations were induced in the thigh muscles of eight healthy volunteers using a pneumatic pressure cuff, both under passive conditions and during isometric muscle contractions. An iterative reconstruction approach based on the Spectro-Dynamic MRI framework was formulated for joint reconstruction of time-resolved 3D images and velocity fields from highly undersampled k-space data at 1.4 Hz. The accuracy of the results was evaluated against fully sampled images, acquired under static conditions with similar deformations. Octahedral shear strain (OSS) values were computed from the estimated motion fields. Mean OSS values were calculated for all thigh muscles, and differences in the mean OSS values between passive and isometric contraction conditions were assessed.

Results: The reconstructed time-resolved images closely matched the fully sampled validation images and the estimated motion fields accurately captured the deformations. Isometric muscle contraction resulted in reduced displacements and lower mean OSS values compared with the passive condition. The largest reduction in mean OSS value was consistently observed in the hamstring muscles, which become stiffer during isometric knee flexion.

Conclusion: Our proposed reconstruction approach enables robust time-resolved 3D strain estimates in muscles using data from a single motion repetition. This method provides new opportunities for investigating the temporal evolution of in vivo displacements and strains in a dynamic setting.

1 | Introduction

MRI is a noninvasive imaging modality that provides excellent soft-tissue contrast, making it a valuable tool for the evaluation of joints and skeletal muscles [1]. Conventional MRI is static, but even a series of static images does not fully capture the dynamic physiological processes during motion [2]. In contrast, dynamic MRI enables the visualization and quantification of motion, deformation, and biomechanical properties of muscle tissue during movement. As such, dynamic MRI has the potential to enhance diagnostic assessments and to deepen the understanding of muscle function [3].

Muscle contractions and deformations can involve complex three-dimensional motion that are only partially captured by two-dimensional imaging methods. 3D imaging techniques are

This is an open access article under the terms of the Creative Commons Attribution License, which permits use, distribution and reproduction in any medium, provided the original work is properly cited.

© 2026 The Author(s). *Magnetic Resonance in Medicine* published by Wiley Periodicals LLC on behalf of International Society for Magnetic Resonance in Medicine.

therefore preferred, as they provide a more complete depiction of muscle kinematics and mitigate artifacts caused by through-slice motion. However, 3D dynamic (3D + t) MRI remains challenging due to prolonged scan times. Thus, advanced acquisition and reconstruction techniques are essential to enable fast time-resolved 3D imaging [4–6].

Besides anatomical imaging, quantifying tissue strain can provide additional insights into the biomechanics of muscle motion [7]. Strain imaging can offer insights into changes in muscle function that are not visible on conventional anatomical MRI images. Muscle strain and strain rates have been measured using techniques including tagging [8, 9], displacement encoding with stimulated echoes (DENSE) [10–12], and phase-contrast-based methods [13–17]. In order to acquire enough data, particularly for 3D acquisitions, these approaches require repeated execution of the motion task, typically dozens of repetitions. However, achieving consistent motion across many repetitions is challenging and requires either a high degree of subject cooperation or the use of electrical muscle stimulation [14]. Moreover, it is not possible to study temporal changes in biomechanical properties during sustained exercise with this approach. These limitations motivate the development of methods capable of inferring time-resolved 3D dynamic information from aperiodic motion, thereby enabling a more accurate representation of muscle dynamics.

Recently, we introduced Spectro-Dynamic MRI as a method for the simultaneous estimation of time-resolved images, deformation fields, and mechanical parameters from highly undersampled data without assuming periodic motion. We demonstrated this technique using 2D data acquired using a moving phantom with piecewise rigid motion [18, 19]. In this work, we extend and adapt the Spectro-Dynamic MRI framework by: (1) extending our acquisition and reconstruction to obtain time-resolved 3D + t images and deformable motion fields; (2) deriving local strain tensor values; and (3) applying our method in vivo. Controlled external deformations were induced in the upper-leg muscles of eight healthy volunteers using a pressure cuff, both under passive conditions and during isometric muscle contractions. Time-resolved reconstructions were performed at a temporal resolution of 1.4 Hz from data acquired during continuous motion. This experimental design enabled the validation of images and motion fields estimated from highly undersampled data using separately acquired static reference images. Finally, we calculated time-dependent strain tensor values from the motion fields, with the aim of showing that changes in these strain values reflect changes in the underlying biomechanical properties of the muscle tissue.

2 | Theory

The Spectro-Dynamic MRI reconstruction [18] is formulated as a joint optimization problem that simultaneously estimates time-resolved images and velocity fields directly from the measured k-space data. It contains the following three terms: a data consistency term $\mathcal{D}$ enforcing agreement between the reconstructed images and the measured k-space data, a motion model term $\mathcal{M}$ linking the time-resolved images to the velocity fields, and a regularization term on the motion fields $\mathcal{R}$. Each component is described in the following subsections.

2.1 | Data Consistency

The k-space data $y_j(\mathbf{k}, t)$ at the spatial frequency $\mathbf{k}$ and time t acquired by the jth receive coil can be modeled as:

$$y_j(\mathbf{k}, t) = \int_{\Omega} m(\mathbf{x}, t) s_j(\mathbf{x}) e^{-2\pi i \mathbf{k}\cdot\mathbf{x}} \, d\mathbf{x}, \tag{1}$$

with $\mathbf{x}$ the spatial coordinate, Ω the image domain, $m(\mathbf{x}, t)$ the complex-valued magnetization or proton density, $s_j(\mathbf{x})$ the coil sensitivity map, and i the imaginary unit.

The data consistency term is now formed by the residual between the discretized forward model and the measured k-space samples $\mathbf{y}_j$:

$$\mathcal{D}(\mathbf{m}) = \sum_j \frac{1}{2} \| W \left(P F S_j \mathbf{m} - \mathbf{y}_j \right) \|_2^2, \tag{2}$$

where $\mathbf{y}_j$ is a vector containing all measured k-space samples for the jth receive coil, $\mathbf{m}$ is a vectorized version of the dynamic time-resolved image, S_j contains the jth coil sensitivity map, F represents the discrete Fourier operator, P is a sampling operator that selects the acquired k-space locations, and W is a diagonal sampling density compensation operator that improves the convergence rate of the reconstruction [20].

2.2 | Motion Model

When motion occurs during the scan, the magnetization changes over time. Under steady-state conditions and in the presence of sufficiently smooth magnetic fields, the total magnetization is conserved during motion. We can describe this conservation of magnetization using the continuity equation [21]:

$$\frac{\partial m}{\partial t} + \nabla \cdot (m\mathbf{v}) = 0, \tag{3}$$

where $\mathbf{v}$ is the Eulerian velocity field. The motion model term is now defined as the residual of the discretized version of (3):

$$\mathcal{M}(\mathbf{m}, \mathbf{v}) = \frac{1}{2} \left\| D_t \mathbf{m} + \sum_d D_x^d \left(\mathbf{m} \odot R_d \mathbf{v} \right) \right\|_2^2, \tag{4}$$

with D_t the temporal finite difference operator, D_x^d the spatial finite difference operator in dimension d, $\mathbf{v}$ the velocity field sampled at the same spatio-temporal locations as $\mathbf{m}$, R_d an operator selecting the velocity vector elements along the dth dimension, and $\odot$ elementwise multiplication.

Note that this velocity-based motion model compares frames locally in time as opposed to relying on warping each frame to a static reference frame, like related displacement-based methods [6, 22, 23].

2.3 | Regularization

The estimation of motion from moving images is an inherently underdetermined problem [24]. Therefore, we need to add additional regularization to prevent implausible motion fields. We do

15222594, 0, Downloaded from https://onlinelibrary.wiley.com/doi/10.1002/mrm.70658 by Centrum Voor Wiskunde En Info (Cwi), Wiley Online Library on [10/11/2026]. See the Terms and Conditions (https://onlinelibrary.wiley.com/terms-and-conditions) on Wiley Online Library for rules of use; OA articles are governed by the applicable Creative Commons License

this by parameterizing the velocity field using smooth B-splines in the spatial dimensions such that $\mathbf{v} = B\mathbf{v}_b$, where B contains the spline basis functions and $\mathbf{v}_b$ are the corresponding spline coefficient, thereby greatly reducing the number of unknown variables. In addition, we add a Tikhonov regularization on the spline coefficients:

$$\mathcal{R}(\mathbf{v}_b) = \frac{1}{2} \| \mathbf{v}_b \|_2^2 \tag{5}$$

2.4 | Iterative Reconstruction

Combining all the terms from the previous subsections, we can formulate a minimization problem that jointly estimates the time-resolved image series $\mathbf{m}$ and the spline coefficients of the velocity field $\mathbf{v}_b$:

$$\min_{\mathbf{m},\mathbf{v}_b} \mathcal{D}(\mathbf{m}) + \lambda \mathcal{M}(\mathbf{m}, \mathbf{v}_b) + \mu \mathcal{R}(\mathbf{v}_b). \tag{6}$$

This minimization was solved by alternating between optimizing for $\mathbf{m}$ and $\mathbf{v}_b$, as shown in Algorithm1. A multi-scale strategy was employed to speed up the reconstruction time, where first a reconstruction was performed at a lower spatial resolution, which was subsequently used as initialization for a reconstruction at the full spatial resolution. Each resolution level used only the central part of k-space $\mathbf{y}^l$ at increasingly larger support, until all measured data was used at resolution level L.

2.5 | Strain Tensor

Let $\boldsymbol{\phi}(\mathbf{x}, t)$ denote the deformation that maps a material point initially located at $\mathbf{x}$ at $t = 0$ to its new position at time t. The (Lagrangian) displacement field is then given by $\mathbf{u}(\mathbf{x}, t) = \boldsymbol{\phi}(\mathbf{x}, t) - \mathbf{x}$. The corresponding velocity field $\mathbf{v}$ is tangent to $\boldsymbol{\phi}$:

$$\frac{\partial \boldsymbol{\phi}(\mathbf{x}, t)}{\partial t} = \mathbf{v}(\boldsymbol{\phi}(\mathbf{x}, t), t). \tag{7}$$

Note that it is conventient to use an Eulerian description of the velocity field, since the k-space sampling grid is fixed. The spatial gradient of the deformation is called the deformation gradient tensor $\mathbf{F}$:

$$\mathbf{F} = (\nabla \boldsymbol{\phi})^T. \tag{8}$$

Strain is a tensor-valued quantity describing local tissue deformations that is derived from the deformation gradient tensor. Multiple strain definitions exist, each useful in different contexts. We use the logarithmic (or Hencky) strain tensor, defined as:

$$\mathbf{E} = \frac{1}{2} \ln(\mathbf{F}^T \cdot \mathbf{F}), \tag{9}$$

ALGORITHM 1 | Iterative reconstruction.

1: $\mathbf{m}^0, \mathbf{v}_b^0 \leftarrow 0$
2: **for** $l = 1$ to L **do** ▷ Resolution level
3: Select low-resolution k-space data $\mathbf{y}^l$ from $\mathbf{y}$
4: **for** $k = 1$ to K^l **do** ▷ Outer iterations
5: $\mathbf{m}^k \leftarrow \arg\min_{\mathbf{m}} \mathcal{D}(\mathbf{m}) + \lambda \mathcal{M}(\mathbf{m}, \mathbf{v}_b^{k-1})$ ▷ `lsqr`
6: $\mathbf{v}_b^k \leftarrow \arg\min_{\mathbf{v}_b} \lambda \mathcal{M}(\mathbf{m}^k, \mathbf{v}_b) + \mu \mathcal{R}(\mathbf{v}_b)$ ▷ `lsqr`
7: **end for**
8: **end for**

For small strains, this strain tensor linearizes to the infinitesimal strain tensor ($\boldsymbol{\varepsilon} = \frac{1}{2}(\mathbf{F} + \mathbf{F}^T) - \mathbf{I}$), while allowing for the generalization of constitutive relations developed for the small-strain regime to moderate strains [25, 26].

The magnitude of the local deformation was quantified using the octahedral shear strain (OSS):

$$\mathrm{OSS} = \frac{2}{3} \sqrt{(E_1 - E_2)^2 + (E_2 - E_3)^2 + (E_1 - E_3)^2}, \tag{10}$$

where E_1, E_2, and E_3 are the principal strains (the eigenvalues of the strain tensor). The OSS is related to the distortional strain energy, and therefore reflects the amount of volume-preserving shape changes in the tissue.

3 | Methods

3.1 | MRI Data Acquisition

Eight healthy volunteers (3F/5M) were included after providing informed consent. A ninth volunteer was excluded due to excessive inter-scan motion, which compromised the estimation of the coil sensitivity maps. The study was approved by the Institutional Review Board of the UMC Utrecht (NL53099.041.15, METC 15/466). The dataset including k-space data is publicly available [27, 28].

Subjects were placed in supine, feet-first position in the scanner. To minimize bulk motion during and between the scans, the lower legs were supported just below the knees and a velcro strap was used to stabilize the knees. A pneumatic cuff from a manually controlled blood pressure monitor was placed around the subject's right thigh (Figure 1). Inflation of the cuff exerted an external compressive force on the thigh, resulting in time-dependent deformations of the muscles. This experimental setup enabled the acquisition of both fully sampled static validation images and highly undersampled data during continuous motion.

All experiments were performed on a 1.5 T system (Ingenia, Philips Healthcare, Best, The Netherlands). For each subject, the following scans were acquired (Table 1): a Dixon scan, a validation scan, and four dynamic scans. During the validation scan, the pressure in the cuff was increased from 0 to 80 mmHg and decreased back to 0 mmHg in increments of 20 mmHg, resulting in nine fully sampled images. Each dynamic scan was acquired during a single 35-s pressure cycle, during which the pressure was continuously increased from 0 to 80 mmHg, immediately followed by a continuous deflation back to 0 mmHg.

For dynamic scans 2 and 4, the subjects were asked to press their heel into the scanner table, leading to isometric contractions of the muscles responsible for bending the knee joint. Subjects were instructed to exert a force as high as they could sustain for 1 min. This isometric knee contraction changed the biomechanical properties of the muscles in the posterior side of the leg, where the primary knee flexors are located. Since the externally applied pressure remained constant, these mechanical changes were hypothesized to result in different deformation patterns.

15222594, 0, Downloaded from https://onlinelibrary.wiley.com/doi/10.1002/mrm.70658 by Centrum Voor Wiskunde En Info (Cwi), Wiley Online Library on [10/11/2026]. See the Terms and Conditions (https://onlinelibrary.wiley.com/terms-and-conditions) on Wiley Online Library for rules of use; OA articles are governed by the applicable Creative Commons License

Between dynamic scans 2 and 3, the pressure cuff was rotated by approximately 90 degrees. Since the pressure distribution around the cuff was nonuniform, the two cuff orientations produced distinct deformation patterns.

The validation scan and the dynamic scans were acquired with a spoiled gradient echo sequence with TR = 5.4 ms, TE = 2.3 ms, flip angle = 6°, matrix size = 128 × 64 × 64, and a 3.5 mm isotropic resolution. The echo time was chosen such that water and fat signals were out of phase, enhancing the contrast at muscle-fat interfaces.

The validation scan was sampled using a conventional linear sampling pattern. This provided fully sampled data at nine discrete pressure levels against which the time-resolved reconstructions from dynamic scan 1 could be compared.

The dynamic scans were sampled on the same 3D k-space grid using Cartesian acquisition with spiral profile order (CASPR) [29]. This sampling strategy combines an efficient sampling of the 3D k-space with the robust reconstruction of Cartesian sampling. Each pseudo-spiral shot contained 32 readouts, starting with the line through the center of k-space. A total of 256 shots were acquired per dynamic scan, resulting in a total acquisition time of 44 s. Combining all shots resulted in a variable-density sampling pattern, with an oversampled center of k-space, and increasingly undersampled higher spatial frequencies.

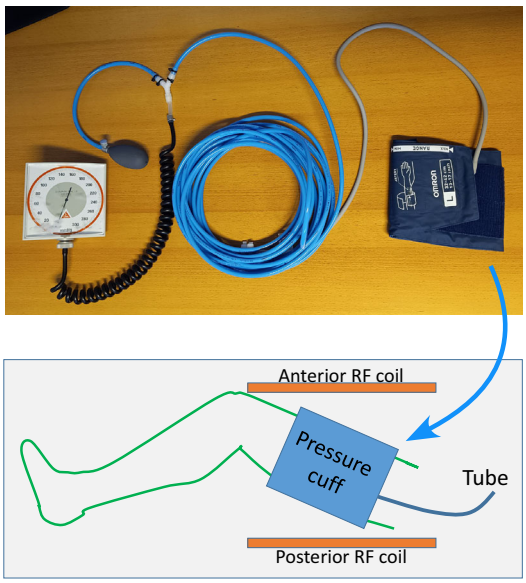


FIGURE 1 | Pressure cuff used to induce deformations in the thigh muscles. Top, from left to right: Pressure gauge, hand pump, long tube (allowing operation outside of the scanner room), and pressure cuff. Bottom: Schematic depiction of the pressure cuff placement around the upper leg.

Segmentation masks of the muscles were automatically determined from the out-of-phase image from the Dixon scan using a pretrained U-Net [30] as implemented in QMRITools [31].

3.2 | Time-Resolved Reconstruction

Both subproblems in Algorithm 1 were solved using the `lsqr` solver, as implemented in Matlab 2025b (The MathWorks Inc., Natick, MA, USA). For line 5, a preconditioner was used to accelerate convergence (Appendix A). Four pseudo-spiral shots were used per reconstructed frame, resulting in a temporal resolution of $4 \times 32 \times 5.4 = 691$ ms, or 1.4 Hz. To speed up the reconstruction time, we used a multi-scale approach with $L = 2$ levels, where the optimization was first performed at half of the nominal spatial resolution in each direction for $K^1 = 15$ outer iterations, followed by $K^2 = 5$ outer iterations at the full spatial resolution. The regularization parameters were determined empirically and set to $\lambda = 100$ and $\mu = 10$ for all reconstructions. The velocity field was parameterized using cubic B-splines with control points on a regular grid with a spacing of 19 mm in each dimension. Spline coefficients corresponding to basis functions whose spatial support lay entirely in the background region were fixed to zero. The reconstruction code is available at github.com/maxvriel/in-vivo-muscle-strain.

3.3 | Validation

Using the data from the validation scan, the reconstruction results from dynamic scan 1 could be evaluated (Figure 2). First, the estimated time-resolved dynamic image series was validated using the fully sampled validation images. Subsequently, the reconstructed images were used to validate the estimated motion fields. All image comparisons were quantified using the structural similarity index measure (SSIM).

TABLE 1 | Overview of the scans acquired for each subject.

Scan name	Sampling	Pressure profile	Purpose	Muscle condition	Cuff position
Dixon scan	Linear	N.A.	Segmentation masks	Passive	N.A.
Validation scan	Linear	9 pressure levels	Fully sampled validation	Passive	Position 1
Dynamic scan 1	CASPR	1 pressure cycle	Dynamic reconstruction	Passive	Position 1
Dynamic scan 2				Isometric contractions	Position 1
Dynamic scan 3				Passive	Position 2
Dynamic scan 4				Isometric contractions	Position 2

15222594, 0, Downloaded from https://onlinelibrary.wiley.com/doi/10.1002/mrm.70658 by Centrum Voor Wiskunde En Info (Cwi), Wiley Online Library on [10/11/2026]. See the Terms and Conditions (https://onlinelibrary.wiley.com/terms-and-conditions) on Wiley Online Library for rules of use; OA articles are governed by the applicable Creative Commons License

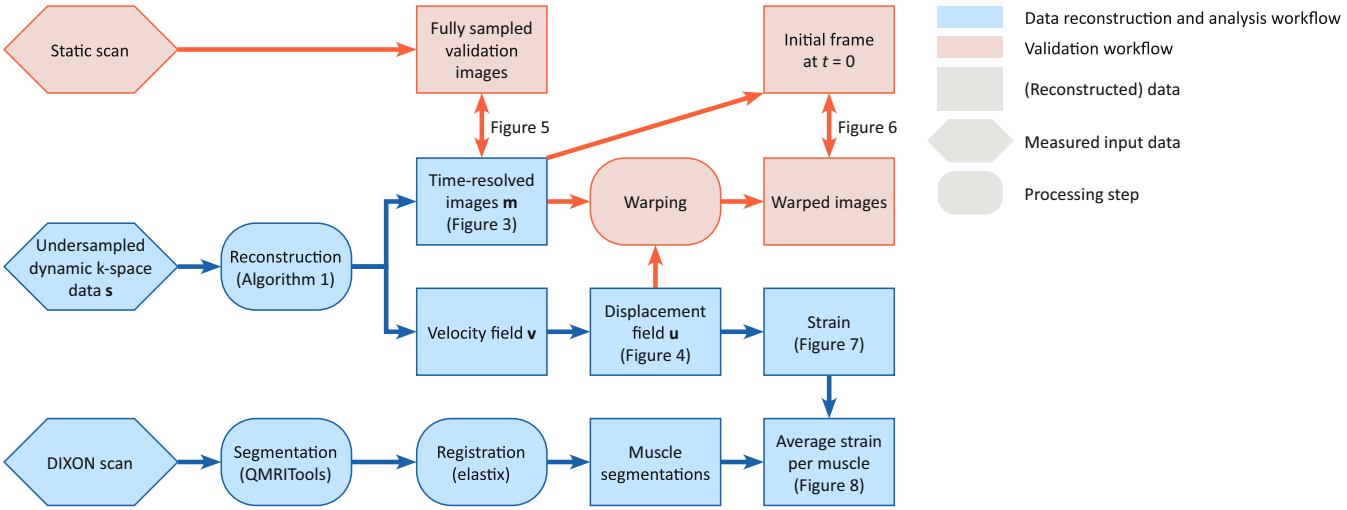


FIGURE 2 | Overview of the reconstruction and analysis workflow. The blue elements show the steps required to generate the main results of this work, while the orange elements depict the validation approach. The mentioned figures show the relevant results or validation steps.

3.3.1 | Image Validation

To validate the reconstructed time-resolved dynamic image series **m**, we compared selected frames from the dynamic reconstructions with the fully sampled validation images. To temporally align the dynamic frames with the static validation images, we used the first readout from each pseudo-spiral shot. After a 1D inverse Fourier transform, this yields the projection of the imaging volume on the readout axis. Equivalent projections were determined for each of the nine validation images, and Pearson's correlation coefficient was calculated for each pair of projections from the dynamic data and the validation data. For each validation image, the dynamic image corresponding to the highest correlation coefficient was selected as the matching dynamic frame. The images were cropped around the right leg and the two images were rigidly registered to each other using `elastix` [32] before calculating the SSIM values to account for minor inter-scan motion. As a baseline reference, the SSIM values were also computed between the first dynamic frame and all validation images, representing the expected similarity when the reconstruction was unable to resolve the motion.

3.3.2 | Motion Field Validation

Based on the reconstructed time-resolved images, the estimated motion fields were evaluated. Lagrangian displacement fields were derived from the reconstructed velocity fields by numerically integrating (7) using a forward Euler scheme and linear spatial interpolation. Each frame of the dynamic image series was spatially warped back to the reference frame using these displacement fields. If the motion fields were estimated correctly, the residual motion in these warped images would be minimal. Baseline reference values were determined by calculating the SSIM without applying any warping, representing the case where the estimated **u** is 0 everywhere.

3.4 | Strain Analysis

OSS values were determined from the displacement fields **u** using finite differences. The muscle segmentation masks derived from the Dixon scan were nonrigidly registered to the reconstructed image in the undeformed state using `elastix` [32]. Mean OSS values were then calculated for each muscle using these segmentation masks. To compare the dynamic scans with passive muscles to those with isometric muscle contractions, the difference in mean OSS value was calculated for each muscle; specifically, between dynamic scans 1 and 2 for the first cuff position, and between dynamic scans 3 and 4 for the rotated cuff position. The scientific color maps lajolla and vik [33] were used to visualize the OSS and OSS differences, respectively.

4 | Results

4.1 | Time-Resolved Reconstruction

Figure 3 shows two orthogonal slices from the reconstructed time-resolved image series at the time point corresponding to the maximal pressure (80 mmHg). The left leg showed no deformation throughout the experiment, whereas the right leg exhibited clear deformations induced by the applied pressure. This is also apparent from the two temporal profiles of the selected image lines, where the left leg showed no change over the course of the experiment, while the right leg showed the increase and decrease of the pressure.

The isometric muscle contractions resulted in smaller deformations given the same external pressure level (Figure 4 and Supplementary Video SV1). To compare the scans with and with-

15222594, 0, Downloaded from https://onlinelibrary.wiley.com/doi/10.1002/mrm.70658 by Centrum Voor Wiskunde En Info (Cwi), Wiley Online Library on [10/11/2026]. See the Terms and Conditions (https://onlinelibrary.wiley.com/terms-and-conditions) on Wiley Online Library for rules of use; OA articles are governed by the applicable Creative Commons License

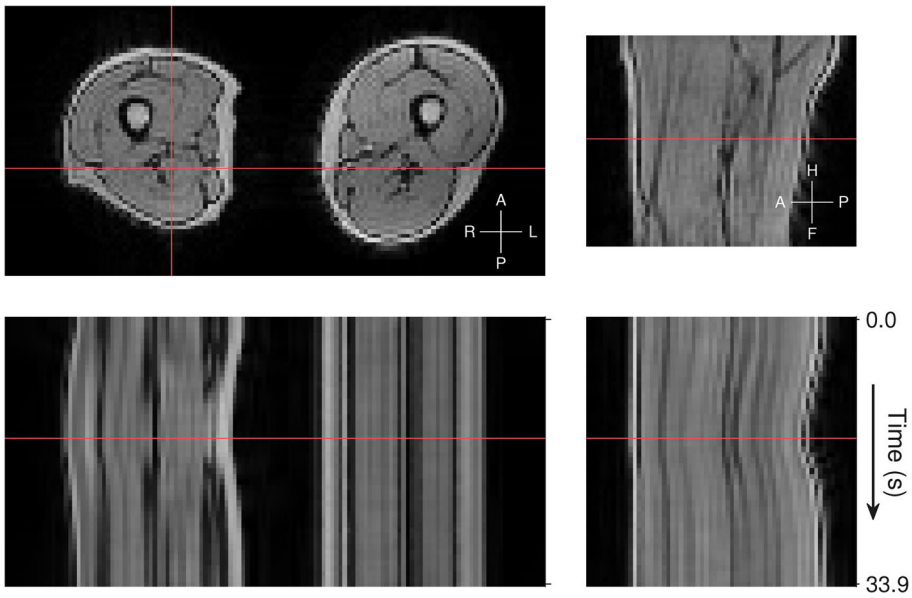


FIGURE 3 | Top: Transverse and sagittal slices from the reconstructed dynamic image series at the time point of maximum deformation. Bottom: Image lines along the RL and AP directions over time. The red lines indicate which lines and time point are depicted in the other views. A: Anterior; P: Posterior; R: Right; L: Left; H: Head; F: Feet.

out isometric contractions, the maximum amplitude of the estimated displacement field was calculated for each scan. This maximum displacement, expressed as mean (min–max) over all volunteers, decreased from 19.4 (13.6–31.4) mm to 13.4 (10.0–17.0) mm. Rotating the pressure cuff resulted in different displacement patterns. Nevertheless, muscle activation again reduced the maximum displacement, from 19.9 (12.6–24.4) mm to 13.2 (8.7–18.3) mm.

4.2 | Validation

4.2.1 | Image Validation

The validation of the reconstructed dynamic image series (Figure 5) showed consistently high SSIM values (>0.80) for all nine time frames and across all eight volunteers. In contrast, the reference values, which were determined by comparing the first dynamic frame to all validation images, exhibited a clear decrease in SSIM as the pressure increases (<0.71), signifying substantial unresolved deformations in the images.

4.2.2 | Motion Field Validation

Based on the reconstructed time-resolved images, the estimated motion fields were evaluated (Figure 5). Warping the dynamic images back to the undeformed reference state resulted in high SSIM values (>0.90). In contrast, not performing any warping (the baseline reference) resulted in substantially lower SSIM values (<0.74). This demonstrates that both the dynamic images and the motion fields accurately capture the motion that occurred during the scan.

4.3 | Strain Analysis

The OSS values showed small deformations in the left leg, while the right leg showed much higher OSS values (Figure 6 and Supplementary Video SV2). The mean OSS value in any muscle of the left leg was smaller than 0.08 across all experiments. For the right leg, the femur showed the smallest mean OSS value in 26 out of the 32 dynamic scans. We observed an overall decrease in mean OSS values during the isometric muscle contractions when compared to the scans under passive conditions (Figure 7), for all volunteers and both cuff positions (Figure 8). The largest reductions in mean OSS values occurred consistently in the muscles located in the posterior part of the thigh (the hamstrings). For example, the mean (min–max) difference in mean OSS value across all volunteers and both cuff positions in the vastus medialis, part of the anterior compartment, was −0.04 (−0.12–0.02), while in the biceps femoris (long head), part of the posterior compartment, it was −0.18 (−0.29 – −0.10).

5 | Discussion

In this work, we have shown that our reconstruction can recover accurate 3D + t images and deformation patterns from undersampled data during continuous aperiodic motion at a temporal resolution of 1.4 Hz. In agreement with the experimental setup, negligible deformation was observed in the contralateral (non-compressed) leg, whereas clear deformation dynamics, consistent with the validation data, were detected in the cuff-compressed leg. The femur, which is expected to be the stiffest tissue in the leg, showed consistently low mean OSS values and was in all cases among the three lowest segmented regions. Moreover, differences between passive and contracted muscle

15222594, 0, Downloaded from https://onlinelibrary.wiley.com/doi/10.1002/mrm.70658 by Centrum Voor Wiskunde En Info (Cwi), Wiley Online Library on [10/11/2026]. See the Terms and Conditions (https://onlinelibrary.wiley.com/terms-and-conditions) on Wiley Online Library for rules of use; OA articles are governed by the applicable Creative Commons License

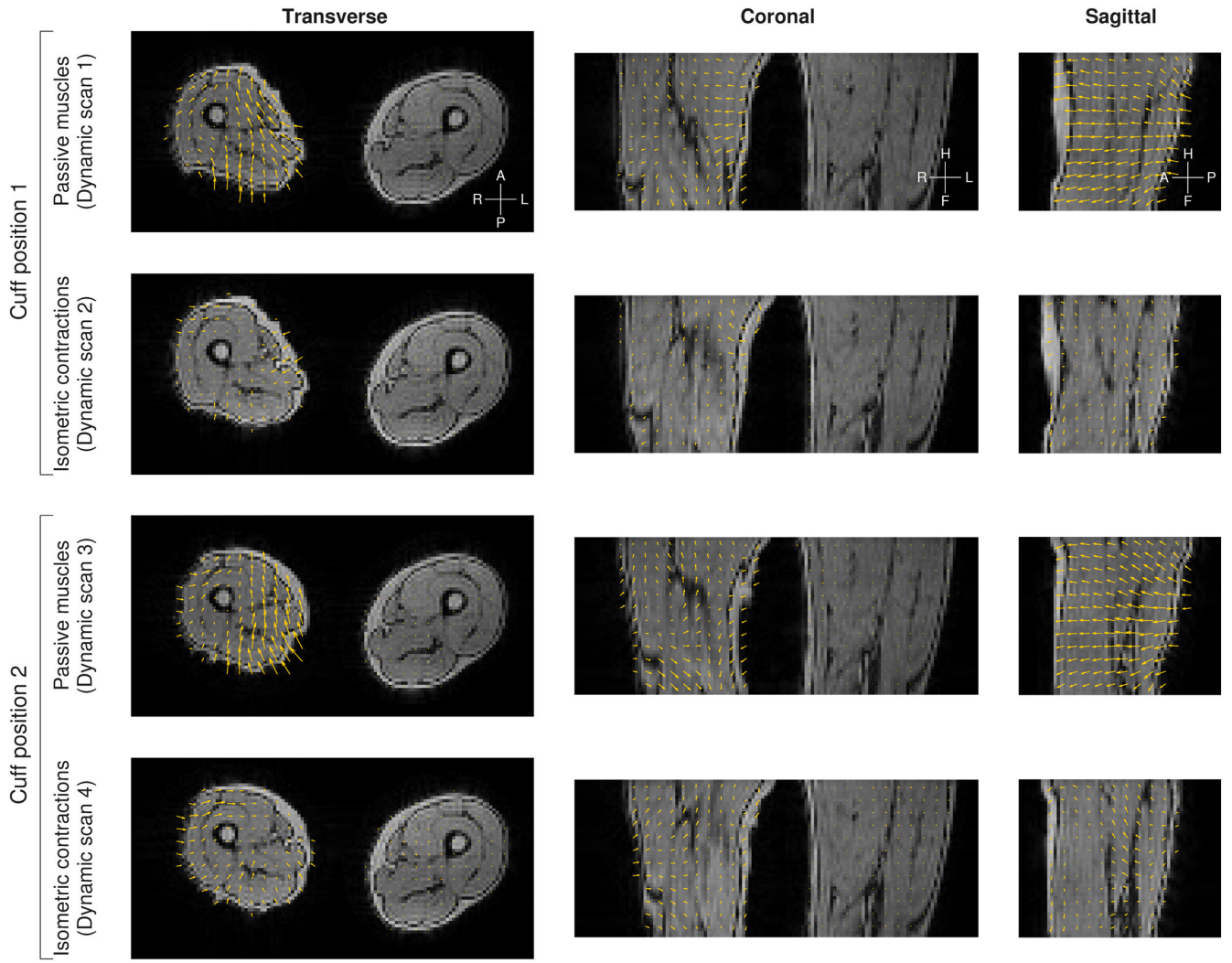


FIGURE 4 | Three-dimensional images and displacement fields at the time point of maximum deformation, for all four dynamic scans, in three orthogonal planes. The pressure cuff was positioned in the initial position for the top two rows, and was rotated for the bottom two rows. The muscles were passive for rows 1 and 3, while an isometric contraction was performed for rows 2 and 4. Note that the deformation fields differ considerably when performing the isometric contraction or when rotating the cuff. An animated version of this figure over time is available as Supplementary Video SV1. A: Anterior; P: Posterior; R: Right; L: Left; H: Head; F: Feet.

conditions were reflected in the magnitude of the displacement fields and derived strain measures, and these differences were consistent across volunteers and different cuff positions.

The hamstring muscles, located at the posterior side of the thigh, function as the primary knee flexors. When activated, these muscles become stiffer, resulting in smaller deformations and lower OSS values when subjected to the same external pressure. The consistent observation of this behavior across all volunteers and cuff positions, despite substantial variability in the deformation patterns, underscores the robustness and validity of the proposed strain estimation approach. It also shows that differences in the measured strain reflect underlying changes in the biomechanical properties of the muscle tissue.

The reconstruction framework proposed in this work (Algorithm 1) alternates between an image reconstruction step (line 5) and a motion estimation step (line 6). Each outer iteration refines the estimate of the time-resolved images, which in turn result in more accurate motion estimations. Although a formal proof of convergence is beyond the scope of this work, empirical observations indicate that the solution stabilizes after only a limited number of outer iterations.

A limitation of our current results is the relatively coarse spatial resolution (3.5 mm isotropic at 1.4 Hz). We expect that improvements in the temporal resolution are possible, but this would require further optimizations in our code to keep reconstruction times and memory requirements under control. Given the trade-off between spatial and temporal resolution, and the flexibility of the CASPR sampling pattern, improvements in temporal resolution can be (partially) leveraged to enhance the spatial resolution in future implementations as well.

Quantitative validation of in vivo strain measurements remains challenging due to the absence of ground truth data. To address this limitation, the experimental protocol was designed to enable indirect validation of the estimated time-resolved images and

15222594, 0, Downloaded from https://onlinelibrary.wiley.com/doi/10.1002/mrm.70658 by Centrum Voor Wiskunde En Info (Cwi), Wiley Online Library on [10/11/2026]. See the Terms and Conditions (https://onlinelibrary.wiley.com/terms-and-conditions) on Wiley Online Library for rules of use; OA articles are governed by the applicable Creative Commons License

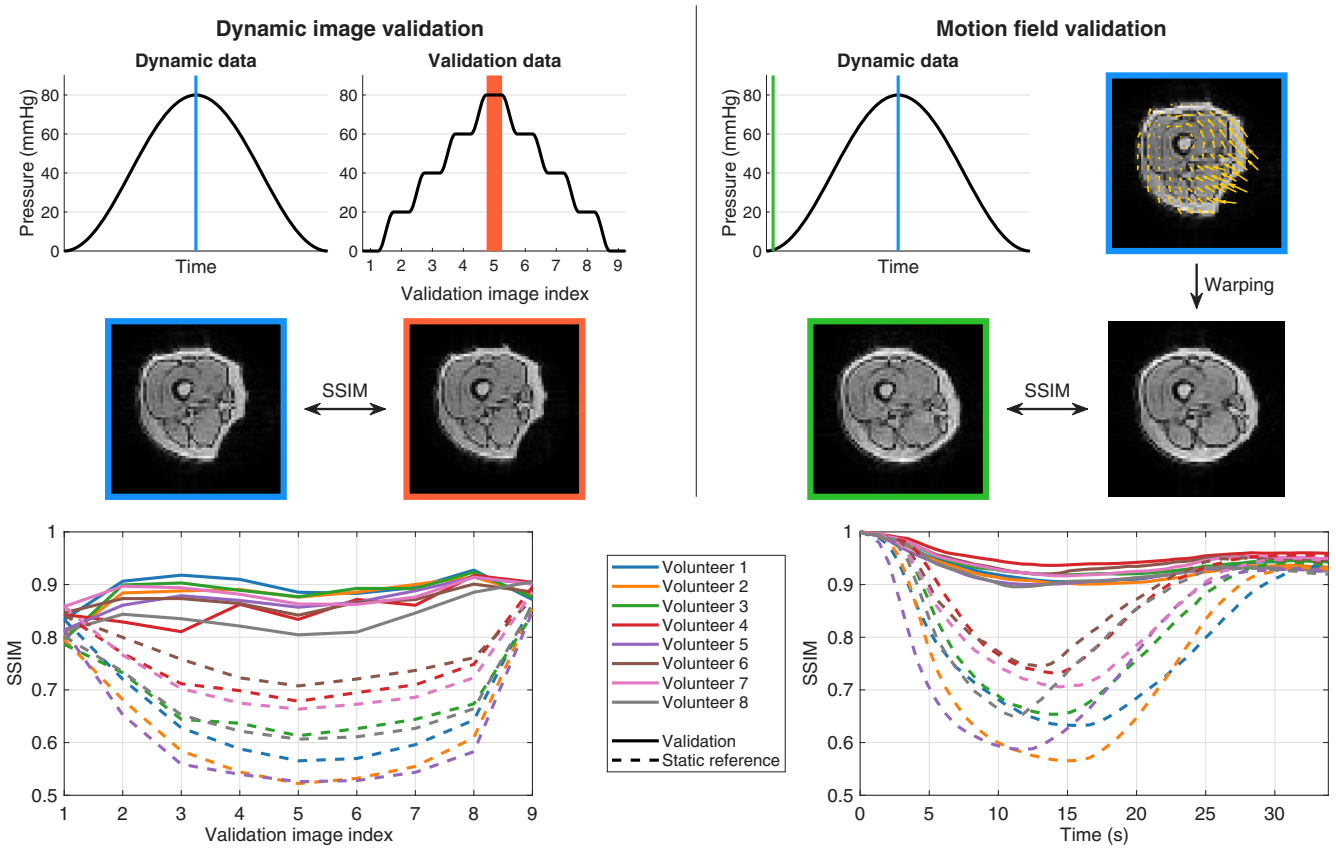


FIGURE 5 | Left: Validation of the time-resolved dynamic image series. During the dynamic scan, the pressure was increased and decreased continuously, while the pressure was fixed during the 22-s acquisition of each validation image. The SSIM values were determined between images from corresponding time points. The graph at the bottom shows the SSIM values for all nine validation time points, across all eight volunteers. Right: Validation of the motion fields. Each frame of the dynamic image series is warped back to the undeformed state using the estimated displacement fields **u**. This image is then compared to the image of the first time frame using the SSIM. The graph shows the SSIM values for all time points across all eight volunteers.

motion fields. However, minor residual error sources may persist in our validation results besides reconstruction-related errors. For instance, validation images and dynamic data were acquired during separate scans, and small positional shifts could have occurred between these scans. Even though we performed a rigid registration to mitigate this, it explains why the SSIM values in Figure 5 for the image validation are slightly lower than those for the motion field validation, where all comparisons are done within the same dynamic scan. Furthermore, the position of the leg after deflation of the pressure cuff might be slightly different from the initial position. These residual misalignments explain why the SSIM values for the motion field validation in Figure 5 do not return to exactly 1. However, the SSIM values do not decrease during the deformations, unlike the reference SSIM values, and the SSIM values after the deflation match the reference values that assume no motion. This suggests that the majority of the motion-related errors are resolved in our reconstruction.

The experimental setup was primarily designed to enable in vivo validation. The use of a pressure cuff as an external deformation source enabled the acquisition of fully sampled data at nine pressure levels, effectively freezing the tissue in nine discrete deformation states. Future studies may use alternative setups, for example by using MR-compatible ergometers, to induce more physiologically relevant motion patterns arising from internal force generation. In addition, this could provide quantitative measurements and control of the force generated during the motion task, resulting in more controlled and reproducible motion.

Alternative analysis strategies may also be explored. For example, the principal strains could be analyzed directly rather than using the octahedral shear strain. In addition, diffusion tensor imaging (DTI)-derived fiber orientations could be incorporated to quantify strain components parallel and perpendicular to the muscle fibers [16]. Additional information may also be obtained from the temporal evolution of the strain values.

The proposed framework creates new opportunities for dynamic imaging in a broad range of applications. For example, it could be a first step towards quantification of time-dependent strain values during muscle activation under dynamic loading or during exercise. Studies in patient populations with musculoskeletal disorders could determine whether differences in strain patterns over time could serve as potential new biomarkers. Applying this work to faster dynamics will likely require additional sources of information or stronger priors to achieve a higher temporal resolution. Potential strategies to deal with the increased undersampling factors include more efficient representations of the images and motion fields [34]. Alternatively, adding velocity-encoding

15222594, 0, Downloaded from https://onlinelibrary.wiley.com/doi/10.1002/mrm.70658 by Centrum Voor Wiskunde En Info (Cwi), Wiley Online Library on [10/11/2026]. See the Terms and Conditions (https://onlinelibrary.wiley.com/terms-and-conditions) on Wiley Online Library for rules of use; OA articles are governed by the applicable Creative Commons License

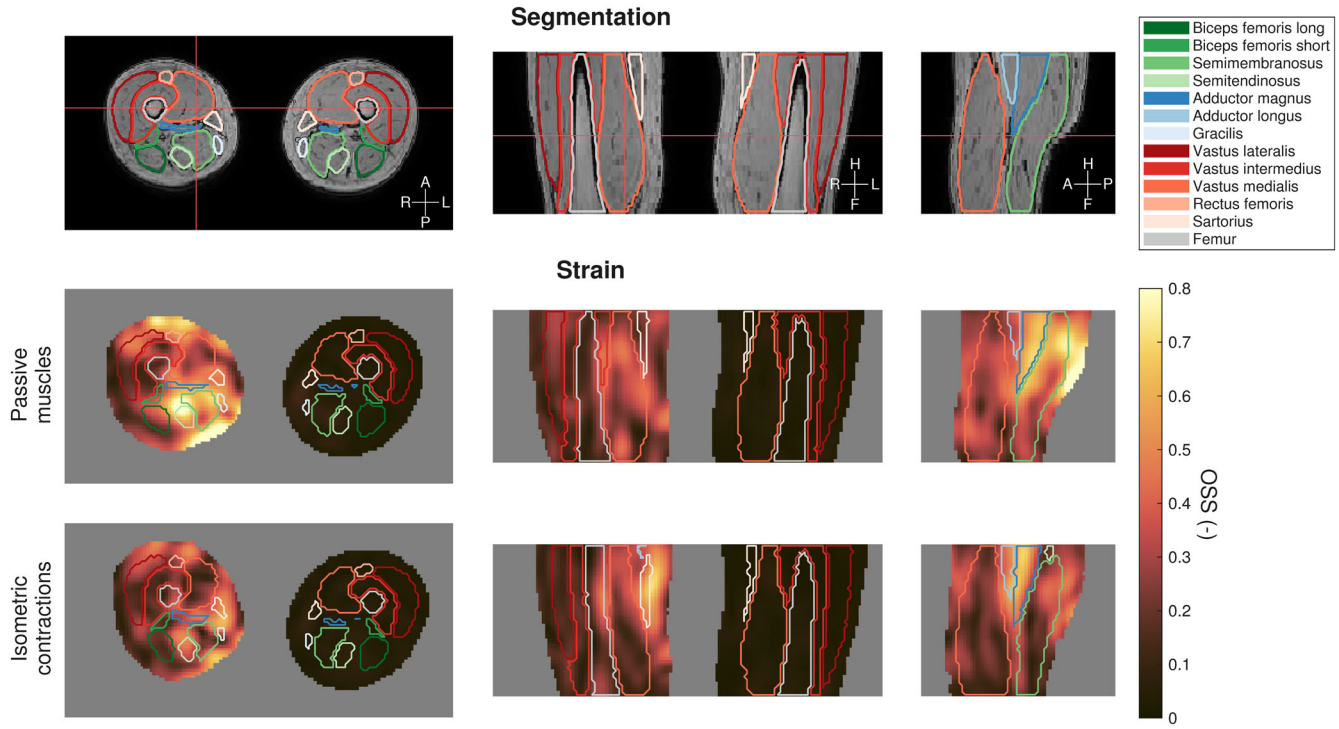


FIGURE 6 | Top: Out-of-phase image from the Dixon scan with the contours of the segmented muscles overlaid on top for volunteer 1. The red lines in each plane show the slices shown in the other two orthogonal planes. Bottom: Octahedral shear strain values for dynamic scans 1 and 2 at the time point of maximum deformation. The segmentations are also given as anatomical reference. Note the absence of strain in the undeformed leg and the decreased strain values during the isometric contraction, especially in the posterior part of the leg. An animated version of this figure over time is available as Supplementary Video SV2. A: Anterior; P: Posterior; R: Right; L: Left; H: Head; F: Feet.

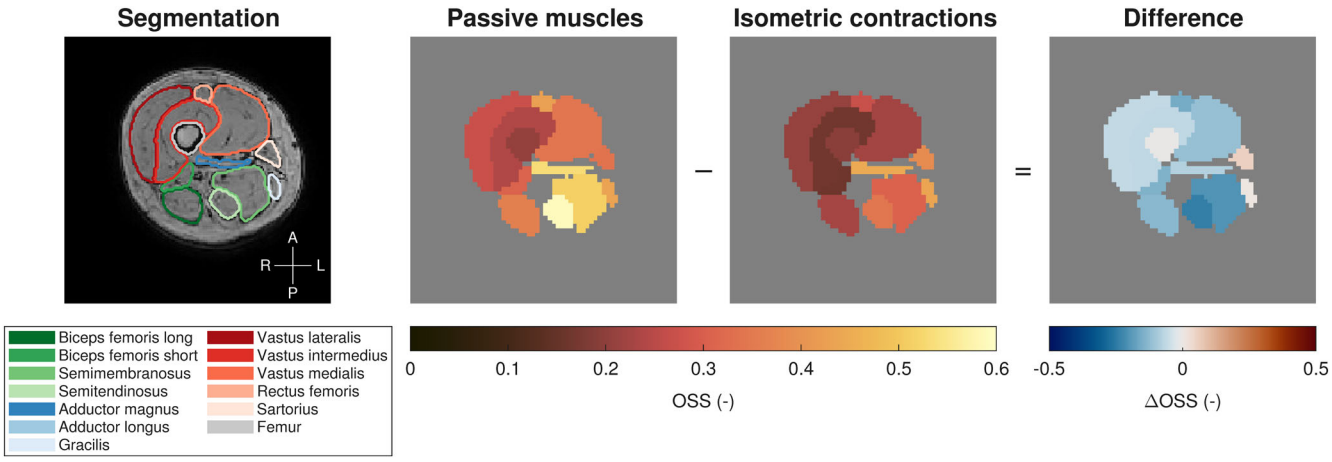


FIGURE 7 | From left to right: Out-of-phase image from the Dixon scan with the contours of the segmented muscles overlaid on top for volunteer 1, mean octahedral shear strain values at the maximum deformation for each segmented muscle in dynamic scans 1 and 2, and muscle-wise differences in mean octahedral shear strain value. Note that the biggest decrease appears in the posterior part of the leg, where the hamstring muscles are located, which are the main knee flexors.

gradients could leverage information about the velocities in the phase of the acquired signal, complementing the velocity estimation using the current framework.

In this work, we have shown that the strain fields reflect biomechanical changes in the muscle tissue. When combined with a biomechanical muscle model, the estimated deformations can be used to infer quantitative biomechanical tissue properties such as stiffness [35]. Combined with a different experimental setup that facilitates physiological motion, this could offer novel opportunities for studying muscle biomechanics in a dynamic setting without requiring motion task repetitions. Additionally, biomechanical models can act as priors in the reconstruction framework by enforcing physically feasible motion fields. These models could

15222594, 0, Downloaded from https://onlinelibrary.wiley.com/doi/10.1002/mrm.70658 by Centrum Voor Wiskunde En Info (Cwi), Wiley Online Library on [10/11/2026]. See the Terms and Conditions (https://onlinelibrary.wiley.com/terms-and-conditions) on Wiley Online Library for rules of use; OA articles are governed by the applicable Creative Commons License

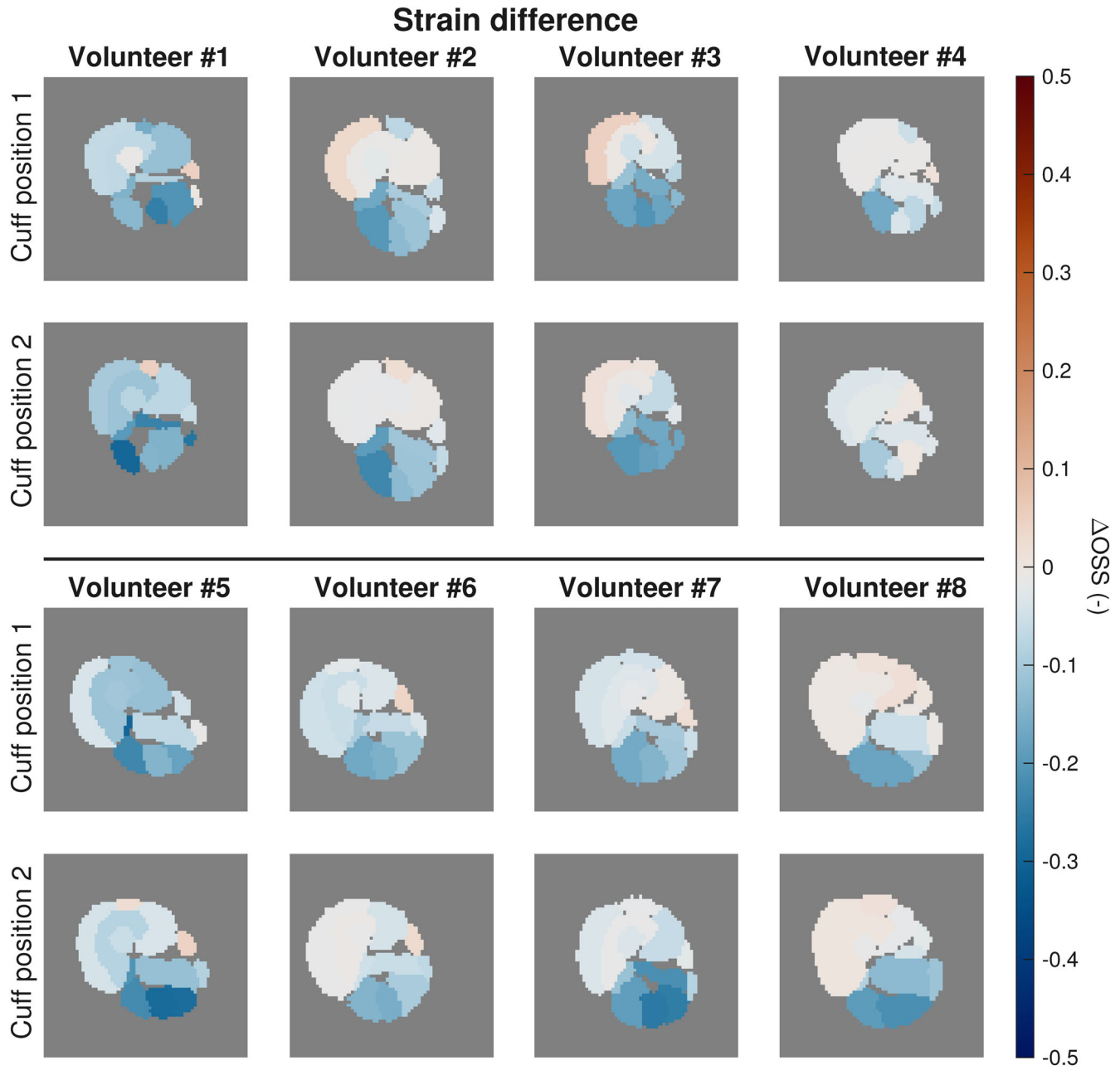


FIGURE 8 | Mean octahedral shear strain difference in the central transverse slice at the maximum deformation over each segmented muscle between the scan with passive muscles and the scan during the isometric contraction. Note that in all cases, the biggest decrease appears in the posterior part of the leg, where the hamstring muscles are located, which are the main knee flexors.

therefore serve as additional regularization, reducing potential biases in the estimated motion fields introduced by the use of B-splines and Tikhonov regularization.

6 | Conclusion

In this work, we demonstrated that time-resolved 3D Spectro-Dynamic MRI enables joint reconstruction of dynamic images and motion fields at 1.4 Hz from highly undersampled data acquired during continuous motion, without assuming periodic motion. In vivo experiments showed deformation patterns that were consistent with the experimental loading conditions. Strain maps derived from the motion fields revealed biomechanical changes during isometric contractions of muscle tissue. The derived strain measures were coherent across volunteers and cuff positioning, supporting the feasibility of the proposed framework for quantitative analysis of muscle biomechanics. These findings indicate that Spectro-Dynamic MRI has potential for investigating biomechanical tissue properties under dynamic conditions.

Acknowledgments

This research was supported by the Dutch Research Council (NWO), grant 18897. The authors would like to thank Ray S.S. Sheombarsing for fruitful discussions. The authors thank the ISMRM Reproducible

15222594, 0, Downloaded from https://onlinelibrary.wiley.com/doi/10.1002/mrm.70658 by Centrum Voor Wiskunde En Info (Cwi), Wiley Online Library on [10/11/2026]. See the Terms and Conditions (https://onlinelibrary.wiley.com/terms-and-conditions) on Wiley Online Library for rules of use; OA articles are governed by the applicable Creative Commons License

Research Study Group for conducting a code review of the code (Version 1.0) supplied in the Data Availability Statement. The scope of the code review covered only the code's ease of download, quality of documentation, and ability to run, but did not consider scientific accuracy or code efficiency.

Funding

This work was supported by Nederlandse Organisatie voor Wetenschappelijk Onderzoek (18897).

Conflicts of Interest

The authors declare no conflicts of interest.

Data Availability Statement

Code to reproduce the reconstructions and figures shown in this paper is openly available on the GitHub repository github.com/maxvriel/in-vivo-muscle-strain/tree/v1.1. The dataset used in this work is openly available on Zenodo at https://doi.org/10.5281/zenodo.21194933.

References

1. D. B. Sneag, F. Abel, H. G. Potter, et al., "MRI Advancements in Musculoskeletal Clinical and Research Practice," *Radiology* 308, no. 2 (2023): e230531, https://doi.org/10.1148/radiol.230531.

2. A. G. d'Entremont, J. A. Nordmeyer-Massner, C. Bos, D. R. Wilson, and K. P. Pruessmann, "Do Dynamic-Based MR Knee Kinematics Methods Produce the Same Results as Static Methods?," *Magnetic Resonance in Medicine* 69, no. 6 (2013): 1634–1644, https://doi.org/10.1002/mrm.24425.

3. B. Borotikar, M. Lempereur, M. Lelievre, V. Burdin, D. B. Salem, and S. Brochard, "Dynamic MRI to Quantify Musculoskeletal Motion: A Systematic Review of Concurrent Validity and Reliability, and Perspectives for Evaluation of Musculoskeletal Disorders," *PLoS One* 12, no. 12 (2017): e0189587, https://doi.org/10.1371/journal.pone.0189587.

4. F. Ong, X. Zhu, J. Y. Cheng, et al., "Extreme MRI: Large-Scale Volumetric Dynamic Imaging From Continuous Non-Gated Acquisitions," *Magnetic Resonance in Medicine* 84, no. 4 (2020): 1763–1780, https://doi.org/10.1002/mrm.28235.

5. L. Feng, "4D Golden-Angle Radial MRI at Subsecond Temporal Resolution," *NMR in Biomedicine* 36, no. 2 (2023): e4844, https://doi.org/10.1002/nbm.4844.

6. T. E. Olausson, M. L. Terpstra, N. R. F. Huttinga, et al., "Free-Running Time-Resolved First-Pass Myocardial Perfusion Using a Multi-Scale Dynamics Decomposition: CMR-MOTUS," *Magnetic Resonance Materials in Physics, Biology and Medicine* 39 (2025): 173–186, https://doi.org/10.1007/s10334-025-01291-x.

7. J. E. Drace and N. J. Pelc, "Skeletal Muscle Contraction: Analysis With Use of Velocity Distributions From Phase-Contrast MR Imaging," *Radiology* 193, no. 2 (1994): 423–429, https://doi.org/10.1148/radiology.193.2.7972757.

8. L. Axel and L. Dougherty, "MR Imaging of Motion With Spatial Modulation of Magnetization," *Radiology* 171, no. 3 (1989): 841–845, https://doi.org/10.1148/radiology.171.3.2717762.

9. K. M. Moerman, A. M. J. Sprengers, C. K. Simms, R. M. Lamerichs, J. Stoker, and A. J. Nederveen, "Validation of Continuously Tagged MRI for the Measurement of Dynamic 3D Skeletal Muscle Tissue Deformation," *Medical Physics* 39, no. 4 (2012): 1793–1810, https://doi.org/10.1118/1.3685579.

10. A. H. Aletras, S. Ding, R. S. Balaban, and H. Wen, "DENSE: Displacement Encoding With Stimulated Echoes in Cardiac Functional MRI," *Journal of Magnetic Resonance* 137, no. 1 (1999): 247–252, https://doi.org/10.1006/jmre.1998.1676.

11. X. Zhong, F. H. Epstein, B. S. Spottiswoode, P. A. Helm, and S. S. Blemker, "Imaging Two-Dimensional Displacements and Strains in Skeletal Muscle During Joint Motion by Cine DENSE MR," *Journal of Biomechanics* 41, no. 3 (2008): 532–540, https://doi.org/10.1016/j.jbiomech.2007.10.026.

12. M. Fiorentino Niccolo, H. Epstein Frederick, and S. Blemker Silvia, "Activation and Aponeurosis Morphology Affect *in Vivo* Muscle Tissue Strains Near the Myotendinous Junction," *Journal of Biomechanics* 45, no. 4 (2012): 647–652, https://doi.org/10.1016/j.jbiomech.2011.12.015.

13. U. Sinha, V. Malis, R. Csapo, A. Moghadasi, R. Kinugasa, and S. Sinha, "Age-Related Differences in Strain Rate Tensor of the Medial Gastrocnemius Muscle During Passive Plantarflexion and Active Isometric Contraction Using Velocity Encoded MR Imaging: Potential Index of Lateral Force Transmission," *Magnetic Resonance in Medicine* 73, no. 5 (2015): 1852–1863.

14. X. Deligianni, M. Pansini, M. Garcia, et al., "Synchronous MRI of Muscle Motion Induced by Electrical Stimulation," *Magnetic Resonance in Medicine* 77, no. 2 (2017): 664–672, https://doi.org/10.1002/mrm.26154.

15. V. Mazzoli, L. M. Gottwald, E. S. Peper, et al., "Accelerated 4D Phase Contrast MRI in Skeletal Muscle Contraction," *Magnetic Resonance in Medicine* 80, no. 5 (2018): 1799–1811, https://doi.org/10.1002/mrm.27158.

16. M. T. Hooijmans, T. T. J. Veeger, V. Mazzoli, et al., "Muscle Fiber Strain Rates in the Lower Leg During Ankle Dorsi−/Plantarflexion Exercise," *NMR in Biomedicine* 37, no. 3 (2024): e5064, https://doi.org/10.1002/nbm.5064.

17. F. Santini, M. G. Croce, X. Deligianni, et al., "Dynamic MR of Muscle Contraction During Electrical Muscle Stimulation: Potential Application to the Evaluation of Neuromuscular Diseases," *NMR in Biomedicine* 38, no. 12 (2025): e70176, https://doi.org/10.1002/nbm.70176.

18. M. H. C. van Riel, T. van Leeuwen, C. A. T. van den Berg, and A. Sbrizzi, "Time-Resolved Reconstruction of Motion, Force, and Stiffness Using Spectro-Dynamic MRI," *IEEE Transactions on Computational Imaging* 9 (2023): 917–927, https://doi.org/10.1109/TCI.2023.3324757.

19. D. G. J. Heesterbeek, M. H. C. van Riel, T. van Leeuwen, C. A. T. van den Berg, and A. Sbrizzi, "Data-Driven Discovery of Mechanical Models Directly From MRI Spectral Data," *IEEE Transactions on Computational Imaging* 10 (2024): 1640–1649, https://doi.org/10.1109/TCI.2024.3497775.

20. K. P. Pruessmann, M. Weiger, P. Börnert, and P. Boesiger, "Advances in Sensitivity Encoding With Arbitrary k-Space Trajectories," *Magnetic Resonance in Medicine* 46, no. 4 (2001): 638–651, https://doi.org/10.1002/mrm.1241.

21. M. H. C. van Riel, N. R. F. Huttinga, and A. Sbrizzi, "Spectro-Dynamic MRI: Characterizing Mechanical Systems on a Millisecond Scale," *IEEE Access* 10 (2022): 271–285, https://doi.org/10.1109/ACCESS.2021.3138631.

22. F. Odille, P.-A. Vuissoz, P.-Y. Marie, and J. Felblinger, "Generalized Reconstruction by Inversion of Coupled Systems (GRICS) Applied to Free-Breathing MRI," *Magnetic Resonance in Medicine* 60, no. 1 (2008): 146–157, https://doi.org/10.1002/mrm.21623.

23. G. Cruz, K. Hammernik, T. Kuestner, et al., "Single-Heartbeat Cardiac Cine Imaging via Jointly Regularized Nonrigid Motion-Corrected Reconstruction," *NMR in Biomedicine* 36, no. 9 (2023): e4942, https://doi.org/10.1002/nbm.4942.

24. B. K. P. Horn and B. G. Schunck, "Determining Optical Flow," *Artificial Intelligence* 17, no. 1 (1981): 185–203, https://doi.org/10.1016/0004-3702(81)90024-2.

25. L. Anand, "On H. Hencky's Approximate Strain-Energy Function for Moderate Deformations," *Journal of Applied Mechanics* 46, no. 1 (1979): 78–82, https://doi.org/10.1115/1.3424532.

15222594, 0, Downloaded from https://onlinelibrary.wiley.com/doi/10.1002/mrm.70658 by Centrum Voor Wiskunde En Info (Cwi), Wiley Online Library on [10/11/2026]. See the Terms and Conditions (https://onlinelibrary.wiley.com/terms-and-conditions) on Wiley Online Library for rules of use; OA articles are governed by the applicable Creative Commons License

26. P. Neff, B. Eidel, and R. J. Martin, "Geometry of Logarithmic Strain Measures in Solid Mechanics," *Archive for Rational Mechanics and Analysis* 222, no. 2 (2016): 507–572.

27. M. H. C. van Riel, D. G. J. Heesterbeek, M. Froeling, C. A. T. van den Berg, and A. Sbrizzi, "An in vivo validation dataset for dynamic volumetric MRI," *Scientific Data* (2026), https://doi.org/10.1038/s41597-026-07939-0.

28. M. H. C. van Riel, D. G. J. Heesterbeek, M. Froeling, C. A. T. van den Berg, and A. Sbrizzi, *An in Vivo Validation Dataset for Dynamic Volumetric MRI* (Zenodo, 2026).

29. C. Prieto, M. Doneva, M. Usman, et al., "Highly Efficient Respiratory Motion Compensated Free-Breathing Coronary Mra Using Golden-Step Cartesian Acquisition," *Journal of Magnetic Resonance Imaging* 41, no. 3 (2015): 738–746, https://doi.org/10.1002/jmri.24602.

30. M. Rohm, M. Markmann, J. Forsting, R. Rehmann, M. Froeling, and L. Schlaffke, "3D Automated Segmentation of Lower Leg Muscles Using Machine Learning on a Heterogeneous Dataset," *Diagnostics* 11, no. 10 (2021): 1747, https://doi.org/10.3390/diagnostics11101747.

31. M. Froeling, "QMRTools: A Mathematica Toolbox for Quantitative MRI Analysis," *Journal of Open Source Software* 4, no. 38 (2019): 1204, https://doi.org/10.21105/joss.01204.

32. S. Klein, M. Staring, K. Murphy, M. A. Viergever, and J. P. W. Pluim, "Elastix: A Toolbox for Intensity-Based Medical Image Registration," *IEEE Transactions on Medical Imaging* 29, no. 1 (2010): 196–205, https://doi.org/10.1109/TMI.2009.2035616.

33. F. Crameri, *Scientific Colour Maps (8.0.1)* (Zenodo, 2023).

34. v. R. M. Sheombarsing Ray, D. Heesterbeek, N. van den Berg, and A. Sbrizzi, "Model-based Dynamic 3D MRI Reconstructions using Neural Fields and Tensor Product Expansions," Version Number: 1 (2026).

35. D. G. J. Heesterbeek, M. H. C. van Riel, R. S. S. Sheombarsing, et al., "Quasi-Static in Vivo Elastography From Internal Displacement Information Only," *Computational Mechanics* 78 (2026): 691–703, https://doi.org/10.1007/s00466-026-02774-x.

Supporting Information

Additional supporting information can be found online in the Supporting Information section. **Video SV1:** Animated version of Figure 4 with each frame showing a different time point. **Video SV2:** Animated version of Figure 6 with each frame showing a different time point.

Appendix A: Preconditioner

The minimization in line 5 of Algorithm 1 is solved using a least squares optimization of the form:

$$\min_{\mathbf{m}} \sum_j \frac{1}{2} \| A_j \mathbf{m} - \mathbf{y}_j \|_2^2 + \frac{\lambda}{2} \| C\mathbf{m} \|_2^2, \tag{A1}$$

with $A_j \mathbf{m} = WPFS_j \mathbf{m}$ from the data consistency term in (2) and $C\mathbf{m} = D_t \mathbf{m} + \sum_d D_x^d (\mathbf{m} \odot \mathbf{v}_d)$ from the motion model term in (4). This leads to the following solution:

$$\mathbf{m} = \left(\sum_j A_j^H A_j + \lambda C^H C \right)^{-1} \sum_j A_j^H \mathbf{y}_j. \tag{A2}$$

To accelerate the convergence of an iterative solver solving (A2), a preconditioner P is introduced which approximates the inverse in (A2). It should strike a balance between being computationally cheap, otherwise evaluating the preconditioner is as expensive as solving the original optimization, and being efficient enough to accelerate the convergence sufficiently. To achieve this trade-off, we use the following two assumptions:

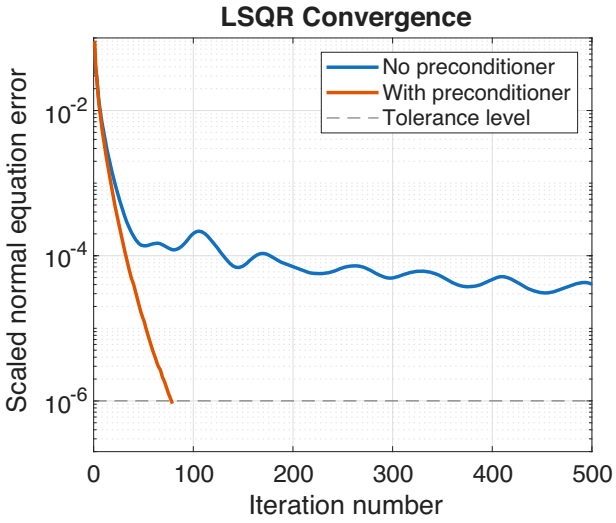


FIGURE A1 | Convergence of the LSQR algorithm in line 5 of Algorithm 1 without and with preconditioner. Both optimizations were performed with the same nonzero values for $\mathbf{v}_b$, as calculated after a single outer iteration with preconditioner. The algorithm reaches the tolerance level after 79 iterations when using the preconditioner, while without preconditioner, the tolerance level has not been reached after 500 iterations.

1. We ignore the effects of the undersampling in (2). Together with the fact that the Fourier transform is a unitary operator, this results in $\sum_j A_j^H A_j \approx \sum_j S_j^H S_j$.
2. We ignore the second term in (4), giving $C^H C \approx D_t^H D_t$. This assumption holds exactly in the first iteration, when $\mathbf{v}_b$ is initialized with zeros.

Note that these approximations are used only in the preconditioner and do not alter the objective function; they only affect the convergence rate of the iterative solver.

The first assumption leads to a time-independent diagonal operator, which is easily inverted. The second assumption results in a convolution with a finite difference kernel in the temporal dimension, which can be diagonalized by the Fourier transform as $D_t^H D_t = F_t^H \Delta F_t$, with F_t the Fourier transform in the temporal dimension only and Δ a diagonal operator. Thus, the preconditioner can be evaluated efficiently by Fast Fourier Transforms and the inversion of a diagonal operator:

$$P = F_t^H \left(\sum_j S_j^H S_j + \lambda \Delta \right)^{-1} F_t. \tag{A3}$$

This preconditioner substantially reduced the number of inner iterations required in line 5 of Algorithm 1 (Figure A1).

15222594, 0, Downloaded from https://onlinelibrary.wiley.com/doi/10.1002/mrm.70658 by Centrum Voor Wiskunde En Info (Cwi), Wiley Online Library on [10/11/2026]. See the Terms and Conditions (https://onlinelibrary.wiley.com/terms-and-conditions) on Wiley Online Library for rules of use; OA articles are governed by the applicable Creative Commons License